Article

Solar-to-hydrogen efficiency of more than 9% in photocatalytic water splitting

Peng Zhou[1], Ishtiaque Ahmed Navid[1], Yongjin Ma[1], Yixin Xiao[1], Ping Wang[1], Zhengwei Ye[1], Baowen Zhou[1], Kai Sun[2] & Zetian Mi[1✉]

Production of hydrogen fuel from sunlight and water, two of the most abundant natural resources on Earth, offers one of the most promising pathways for carbon neutrality[1–3]. Some solar hydrogen production approaches, for example, photoelectrochemical water splitting, often require corrosive electrolyte, limiting their performance stability and environmental sustainability[1,3]. Alternatively, clean hydrogen can be produced directly from sunlight and water by photocatalytic water splitting[2,4,5]. The solar-to-hydrogen (STH) efficiency of photocatalytic water splitting, however, has remained very low. Here we have developed a strategy to achieve a high STH efficiency of 9.2 per cent using pure water, concentrated solar light and an indium gallium nitride photocatalyst. The success of this strategy originates from the synergistic effects of promoting forward hydrogen–oxygen evolution and inhibiting the reverse hydrogen–oxygen recombination by operating at an optimal reaction temperature (about 70 degrees Celsius), which can be directly achieved by harvesting the previously wasted infrared light in sunlight. Moreover, this temperature-dependent strategy also leads to an STH efficiency of about 7 per cent from widely available tap water and sea water and an STH efficiency of 6.2 per cent in a large-scale photocatalytic water-splitting system with a natural solar light capacity of 257 watts. Our study offers a practical approach to produce hydrogen fuel efficiently from natural solar light and water, overcoming the efficiency bottleneck of solar hydrogen production.

Bias-free unassisted photocatalytic overall water splitting (OWS) into hydrogen (H_2) and oxygen (O_2) at a stoichiometric ratio of 2:1 is desirable for long-term clean, renewable and sustainable fuel production on Earth[1–3]. Compared with the extensively studied photoelectrochemical water splitting[6–8], photocatalytic OWS does not require the use of conductive electrolyte, for example, strongly acidic or alkaline solutions[2]. Instead, fresh water, or sea water, can be readily split into H_2 and O_2 via photocatalytic OWS without any external bias or circuitry, which can significantly reduce the system cost and mitigate photocatalyst corrosion, stability and safety-related issues[2,4,5]. The major challenges for photocatalytic OWS, however, are directly related to the narrow visible-light-response range, severe photogenerated electron–hole recombination, high surface catalytic overpotential and the undesirable recombination of produced hydrogen and oxygen of common photocatalyst materials, leading to a limited solar-to-hydrogen (STH) efficiency (less than about 3%) in most reported photocatalytic systems[9–11]. The light-response range of a photocatalyst directly determines its theoretical maximum STH efficiency. Although an external quantum efficiency of 96% has been reported under ultraviolet light (350–360 nm) illumination for aluminium-doped strontium titanate in photocatalytic OWS, the total content of ultraviolet light (300–400 nm) in the natural solar spectrum is less than 3% (ref. [12]). Nearly 40% of solar light lies in the visible spectrum (400–700 nm), which can theoretically contribute to a STH efficiency of 24% in photocatalytic OWS[13]. However, the currently reported visible-light-responsive catalysts are generally restricted to 400–485 nm with limited energy conversion efficiency[9,14]. In addition to ultraviolet and visible light, the content of infrared light in the solar spectrum reaches up to 50%. Infrared light, however, cannot directly photo-excite the catalyst to produce electrons and holes with sufficient energy to drive OWS, which limits the maximum achievable STH efficiency in photocatalytic OWS. Hence, an effective strategy that can potentially utilize the full solar spectrum for photocatalytic OWS is expected to substantially improve STH efficiency[15].

Recently, indium gallium nitride (InGaN)/gallium nitride (GaN) nanowire (NW) photocatalysts with high crystallinity have been controllably grown on commercial silicon wafers, which have shown a wide visible-light-response range (400–700 nm) and suitable band-edge potentials for OWS[16,17]. Substantial progress has also been made on tuning the surface band structure, internal electric field and cocatalysts to improve STH efficiency[9,14,18]. Hence, InGaN/GaN NW photocatalysts provide a suitable platform to achieve high-efficiency photocatalytic water splitting. Here we report an observable temperature-dependent hydrogen–oxygen recombination effect in photocatalytic OWS on rhodium (Rh)/chromium oxide (Cr_2O_3)/cobalt oxide (Co_3O_4)-loaded InGaN/GaN NWs. Guided by this finding, we propose a high-efficiency reaction mechanism and successfully demonstrate an STH efficiency

[1]Department of Electrical Engineering and Computer Science, University of Michigan, Ann Arbor, MI, USA. [2]Department of Materials Science and Engineering, University of Michigan, Ann Arbor, MI, USA. ✉e-mail: ztmi@umich.edu
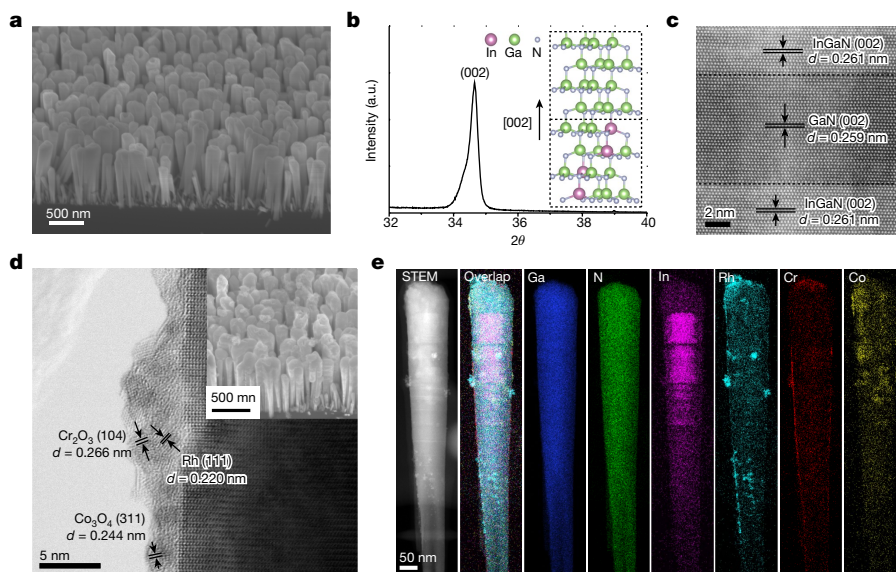
Fig. 1 | Structure characterization. a, A 45°-tilted FESEM image of the InGaN/GaN NWs. **b**, XRD pattern of the InGaN/GaN NWs. **c**, STEM image of the InGaN/GaN heterostructure. **d**, HRTEM of the supported Rh/Cr$_2$O$_3$/Co$_3$O$_4$ cocatalyst on the InGaN/GaN NWs. Inset: FESEM of the Rh/Cr$_2$O$_3$/Co$_3$O$_4$-loaded InGaN/GaN NWs. **d**, the distance between successive, parallel planes. **e**, STEM and element mapping of the Rh/Cr$_2$O$_3$/Co$_3$O$_4$-loaded InGaN/GaN NWs.

of about 9.2% for the photocatalytic OWS reaction, which is attributed to the enhanced forward hydrogen–oxygen evolution reaction and the inhibited hydrogen–oxygen recombination reaction at an optimal reaction temperature (about 70 °C). In addition, guided by this strategy, an STH efficiency of 6.2% was achieved on a large-scale photocatalytic OWS system with a high, concentrated natural solar light intensity of about 16,070 mW cm^{-2} on a 4 cm × 4 cm photocatalyst wafer, showing the feasibility of InGaN/GaN-based solar hydrogen technology from the lab for practical application.

InGaN/GaN NWs supported on silicon wafer were synthesized by molecular-beam-epitaxy technology in this study[14,19]. The field-emission scanning electron microscopy (FESEM) image showed the well arrayed InGaN/GaN NWs with a length of about 1.2 μm on silicon wafer (Fig. 1a). The X-ray diffraction (XRD) pattern and high-angle annular dark-field scanning transmission electron microscopy (HAADF-STEM) image indicated the high crystallinity of InGaN/GaN NWs, which were grown along the [002] direction according to the standard powder diffraction file (2–1078) of Ga(In)N (Fig. 1b,c). In addition, it was observed that GaN with a thickness of about 10 nm acted as the cap layer to support InGaN, indicating a controllable atomic configuration for the InGaN/GaN NWs (Fig. 1c). The Rh/Cr$_2$O$_3$ core/shell and Co$_3$O$_4$ nanoparticles (shown in Fig. 1d) were photo-reduced on the InGaN/GaN NWs, and acted as the cocatalysts for hydrogen and oxygen production, respectively. Energy-dispersive X-ray (EDX) elemental mapping analysis showed the distribution of Rh, Cr and Co in the whole InGaN/GaN NW (Fig. 1e), and revealed uniform hydrogen- and oxygen-production regions along the whole NW. The contents of Rh, Cr and Co in the InGaN/GaN NWs were examined by an inductively coupled plasma-atomic emission spectrometer (ICP-AES) to be 5.2 μg cm^{-2}, 1.9 μg cm^{-2} and 33.3 μg cm^{-2}, respectively (Extended Data Table 1). Owing to the composition pulling effect, the distribution of In in InGaN/GaN NWs varied along with the growth direction, leading to a large variation of the energy bandgap and therefore broad-band light absorption. This was confirmed by SEM-cathodoluminescence (SEM-CL) measurements (Extended Data Fig. 1). In addition, ultraviolet–visible diffuse reflectance spectroscopy (DRS) showed three peaks at 408 nm, 494 nm and 632 nm in the full visible spectrum (Extended Data Fig. 2a). On the basis of the function

relationship between the In content and the bandgap of InGaN, the In content in InGaN NWs was calculated to be in the range of 0.09–0.40 (Extended Data Fig. 2b)[16,20]. It is noted that the different InGaN segments could not form the commonly reported heterojunction or Z-scheme charge transfer according to the obtained band diagram (Extended Data Fig. 2b)[21]. Instead, it was considered that the different InGaN segments independently worked in the charge carrier separation and transfer. However, it was considered that the multi-band structure was beneficial to the maximization of the redox ability of the photogenerated electrons and holes, which could accelerate the rate of photocatalytic reaction[17]. In particular, the bandgap corresponding to 632 nm could theoretically contribute to a maximum STH efficiency of 17.7% under natural solar light and 31.1% under simulated solar light from a xenon (Xe) lamp with the incorporation of an AM1.5G filter (Extended Data Fig. 2c,d).

First, a temperature-controllable photocatalytic system was designed to perform OWS in pure water at different temperatures ranging from 30 °C to 80 °C under the same concentrated simulated solar light (3,800 mW cm^{-2}; Extended Data Fig. 3a,b and Extended Data Table 2). The STH efficiency of the Rh/Cr$_2$O$_3$/Co$_3$O$_4$-loaded InGaN/ GaN NWs showed a remarkable dependence on the operating temperature of the system, which increases significantly with temperature (Fig. 2a). The STH efficiency reached a maximum value (8.8%) at 70 °C by varying cocatalyst content and light intensity (Extended Data Fig. 3c,d). However, further increasing the temperature to 80 °C did not improve the STH efficiency. Hence, the temperature is a curial factor determining the STH efficiency of photocatalytic OWS on the present Rh/Cr$_2$O$_3$/Co$_3$O$_4$-loaded InGaN/GaN NWs. Guided by this finding, a heat-insulating-layer-equipped system was designed to directly utilize the infrared light of the solar spectrum to heat the system to about 70 °C (Extended Data Fig. 4a,b), which avoided any additional energy consumption for maintaining the temperature of the reaction system (Extended Data Fig. 4c–e). The obtained results showed that the incorporation of a heat-insulating layer enabled the system to operate at a temperature of about 70 °C. In a 74-hour test, an STH efficiency of 9.2% using pure water was obtained under concentrated simulated solar light (3,800 mW cm^{-2}; Fig. 2b, Extended Data Fig. 5a
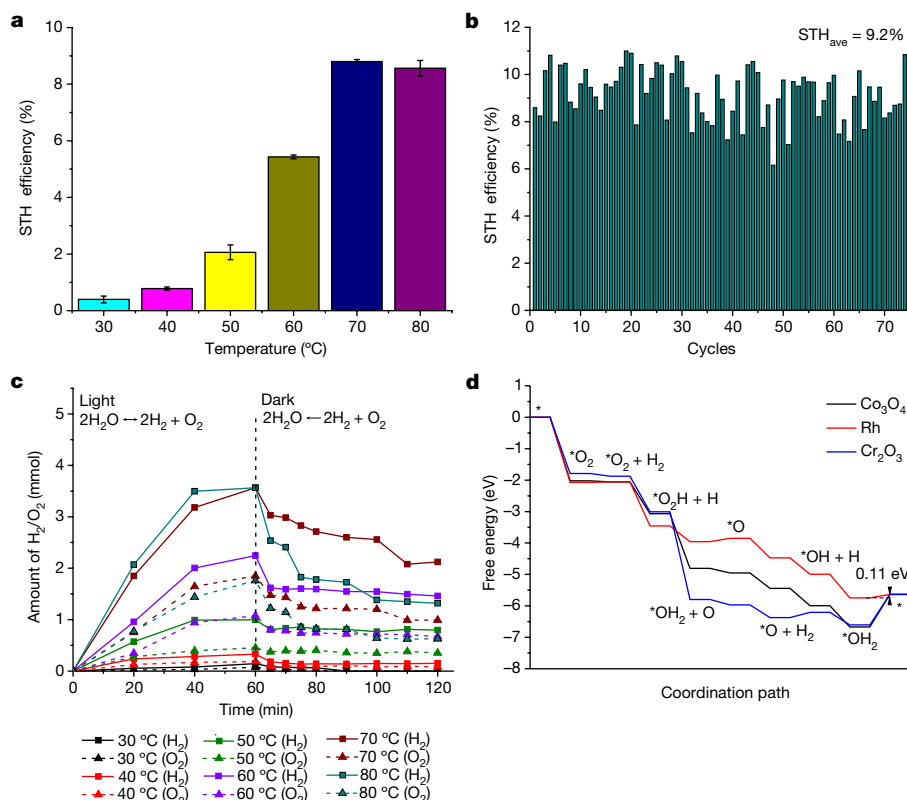
Fig. 2 | Performance evaluation and mechanism analysis. a, Temperature-dependent STH efficiency of the Rh/Cr$_2$O$_3$/Co$_3$O$_4$–InGaN/GaN NWs. A 300-W Xe lamp equipped with an AM1.5G filter was used to produce concentrated light of 3,800 mW cm^{-2} on a 0.8 cm × 0.8 cm Rh/Cr$_2$O$_3$/Co$_3$O$_4$-loaded InGaN/GaN NW wafer. **b**, Stability test of the Rh/Cr$_2$O$_3$/Co$_3O_4$-loaded InGaN/GaN NWs in the self-heated photocatalytic OWS system (Extended Data Fig. 4) under concentrated light of 3,800 mW cm^{-2}. Each cycle is 1 hour. **c**, Temperature-dependent hydrogen–oxygen recombination reaction. **d**, Free-energy profile of hydrogen–oxygen recombination on the cocatalyst Co$_3$O$_4$, Rh and Cr$_2$O$_3$. Error bars indicate standard deviation for three measurements.

and Extended Data Table 3). The turnover frequency (TOF) and turnover number (TON) were calculated to be 601 h^{-1} and 44,458 in the 74-hour test, respectively. It is noted that the activity of the Rh/Cr$_2$O$_3$/Co$_3$O$_4$-InGaN/GaN NWs decreased by 26% in a further 6-hour test (Extended Data Fig. 5b), indicating the partial deactivation of photocatalyst. According to the SEM analysis after reaction, the thickness of the InGaN/GaN NWs was still maintained at about 1.2 μm, indicating little loss of the InGaN/GaN photocatalyst (Extended Data Fig. 5c). In addition, the HRTEM analysis indicated that the crystal structure of the InGaN/GaN photocatalyst and the distribution of the Rh/Cr$_2$O$_3$/Co$_3$O$_4$ cocatalyst were the same as before the reaction (Extended Data Fig. 5d,e). However, the ICP tests on the cocatalyst contents after and before reaction (Extended Data Table 1) showed that the Rh and Co contents decreased by 50%, which is a common phenomenon for the deactivation of photocatalyst after a long-term test[22]. Hence, the decrease in the STH efficiency after the 74-h stability test is primarily owing to the loss of cocatalysts. As a comparison, the photocatalytic OWS was also performed without a heat-insulating layer, which yielded a reaction temperature of only 50.8 °C and an STH efficiency of about 2–3% (Extended Data Fig. 6a,b). This clearly demonstrated the feasibility of a temperature-control strategy for significantly improving the STH efficiency on Rh/Cr$_2$O$_3$/Co$_3$O$_4$–InGaN/GaN NWs.

In general, increasing the reaction temperature can enhance mass transfer and chemical bond formation and breaking in a catalytic reaction, thus contributing to a higher reaction rate[23–25]. By using methanol as an electron donor and potassium iodate (KIO$_3$) as an electron acceptor in photocatalytic water splitting, it was found that both the half hydrogen-production and oxygen-production rates were

significantly improved with reaction temperature (Extended Data Fig. 6c,d). However, the difference was that the oxygen-production rate was not further improved with temperatures higher than 70 °C. This implied that further increase of the STH efficiency with temperature was probably limited by the rate-determining oxygen evolution reaction[26–28]. In addition to the forward reaction, the back reaction, that is, hydrogen–oxygen recombination, was another determining factor influencing the maximum achievable STH efficiency. In photocatalytic OWS, hydrogen–oxygen production (2H$_2$O → 2H$_2$ + O$_2$) often competes with hydrogen–oxygen recombination (2H$_2$O ← 2H$_2$ + O$_2$)[29,30]. For example, with increasing hydrogen/oxygen concentration in the present photocatalytic system, the hydrogen–oxygen production and recombination reached a balance (2H$_2$O ↔ 2H$_2$ + O$_2$) (Extended Data Fig. 6e). This strongly indicates a remarkable inhibiting effect of hydrogen–oxygen recombination on the photocatalytic OWS. Although the Rh/Cr$_2$O$_3$ core/shell structure has been reported to potentially reduce hydrogen–oxygen recombination in the photocatalytic OWS, its behaviour at different temperatures has remained unknown[11,31]. A hydrogen–oxygen recombination experiment was designed to investigate the temperature effect on hydrogen–oxygen recombination (Fig. 2c). The stoichiometric hydrogen and oxygen were first produced under the same light irradiation at different temperatures. Then the amounts of hydrogen and oxygen gradually decreased with time at an approximate stoichiometric ratio of 2:1 after the light was removed, directly demonstrating the hydrogen–oxygen recombination. Finally, the contents of hydrogen and oxygen were maintained at certain values. Surprisingly, the balance contents of hydrogen and oxygen varied significantly with temperature. The balance contents of hydrogen and oxygen first increased with temperature and reached the highest value
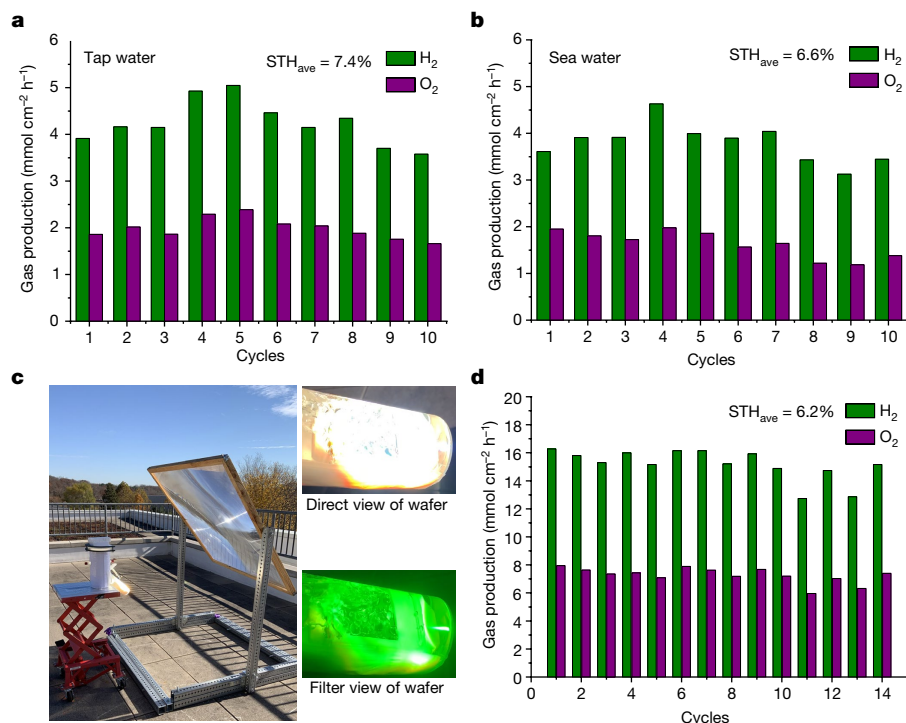
Fig. 3 | Practical and large-scale application. a,b, STH efficiency of Rh/Cr$_2$O$_3$/Co$_3$O$_4$-loaded InGaN/GaN NWs in tap water from Ann Arbor, Michigan, United States (**a**) and sea water simulated by 3.5 wt% NaCl aqueous solution (**b**). The intensity of simulated solar light from a 300-W Xe lamp equipped with an AM1.5G filter was 3,800 mW cm^{-2}. The sample size is 0.64 cm^2. Each cycle is 1 hour. **c,d,** Image of outdoor photocatalytic OWS system on North Campus at the University of Michigan, Ann Arbor, Michigan, United States (**c**) and the corresponding STH efficiency of a 4 cm × 4 cm Rh/Cr$_2$O$_3$/Co$_3$O$_4$-loaded InGaN/GaN NW wafer under concentrated natural solar light (about 16,070 mW cm^{-2}) (**d**). Each cycle is 10 min. The detailed system parameters are shown in Extended Data Fig. 8. The dynamic process of gas (hydrogen, oxygen and vapour) production is shown in Supplementary Video 1 (direct view) and Supplementary Video 2 (filter view). The control experiment with the production of only water vapour by using pristine silicon wafer as the sample is shown in Supplementary Video 3.

at about 70 °C. It is noted that hydrogen and oxygen evolution cannot be directly produced in the dark at 70 °C as the Gibbs free energy of OWS is up to 237,000 J mol^{-1} (Extended Data Fig. 6f). However, further increasing the temperature to 80 °C was found to enhance the recombination of hydrogen and oxygen. A higher balance content suggests a higher tolerance on hydrogen–oxygen contents, which contributes to a reduced hydrogen–oxygen recombination reaction and a stronger ability for the system to support mixed hydrogen and oxygen gas. This well explains the highest photocatalytic OWS activity at 70 °C.

To further investigate the mechanism of temperature-dependent hydrogen–oxygen recombination at the atomic scale, density functional theory (DFT) calculations were used to simulate the reaction pathway on cocatalyst Co$_3$O$_4$, Rh and Cr$_2$O$_3$ (Fig. 2d, Extended Data Fig. 7 and Extended Data Table 4). The results suggested that the energy barrier (0.11 eV) of hydrogen–oxygen recombination on Rh was much less positive than that on Co$_3$O$_4$ (1.03 eV) or Cr$_2$O$_3$ (0.97 eV). Hence, Rh was the main hydrogen–oxygen recombination centre, which is consistent with the speculation of previous experimental studies[11]. More importantly, most steps except water desorption in the hydrogen–oxygen recombination on Rh were typically exothermal. Hence, increasing the temperature of reaction system in a certain range could desirably inhibit hydrogen–oxygen recombination on the Rh cocatalyst. Thus, the hydrogen–oxygen recombination was decreased with increasing temperature from 30 °C to 70 °C. The enhanced hydrogen–oxygen recombination at a higher temperature (80 °C) was attributed to the improved diffusivity coefficient of hydrogen and oxygen caused by further temperature increase accelerating the mass transfer in water, which became dominant in the hydrogen–oxygen recombination reaction[32]. Hence, about 70 °C was the optimal temperature for inhibiting hydrogen–oxygen recombination on the Rh/Cr$_2$O$_3$/Co$_3$O$_4$-InGaN/

GaN NWs in this study. Furthermore, an excessively high temperature may enhance the non-radiative recombination of photogenerated electrons and holes in photocatalyst, which also contributes to the optimal temperature at 70 °C (ref. [33]).

To explore the practicality of temperature-dependent photocatalytic OWS, we also used tap water and sea water, which generated hydrogen and oxygen with an approximate stoichiometric ratio of 2:1, over Rh/Cr$_2$O$_3$/Co$_3$O$_4$–InGaN/GaN NWs at about 70 °C (Fig. 3a,b). The STH efficiency achieved in 10-hour tests was 7.4% and 6.6%, respectively, lower than the 9.2% STH efficiency achieved with deionized water. The reduced efficiency might be the result of ions or other impurities present in tap water and sea water reducing the activity of the photocatalyst material. As using light of higher intensity can in principle decrease material costs (a given irradiated area will receive more light energy and generate more product than systems using one-sun irradiation), we operated a larger and simple water-splitting system consisting of a 4 cm × 4 cm photocatalyst wafer exposed to concentrated solar light (about 16,070 mW cm^{-2}) that delivered 257 W (Fig. 3c and Extended Data Fig. 8a)[10,22]. Outdoor tests showed that the insulating-layer-coated chamber could maintain the optimized operating temperature (75 ± 3 °C) (Extended Data Fig. 8b), and that the photocatalyst wafer remained stable when exposed to the concentrated solar light that had the highest intensity used in photocatalytic OWS (Fig. 3c, Supplementary Videos 1 and 2). During a 140-min test, the system achieved an average STH efficiency of 6.2%, one of the highest values reported so far for photocatalytic water splitting under natural solar light (Fig. 3d and Extended Data Table 3)[22]. The TOF and TON values of InGaN/GaN NWs during this 140-min outdoor test were 24,063 h^{-1} and 56,148, respectively, indicating efficient use of the InGaN/GaN NW photocatalysts. During further outdoor testing, partial loss of cocatalysts reduced

Article

the STH efficiency of the photocatalyst system (Extended Data Fig. 8c and Extended Data Table 1). Although this issue and other challenges remain to be addressed, our findings demonstrate that it is possible to efficiently produce hydrogen using sunlight and tap or sea water.

Online content

Any methods, additional references, Nature Portfolio reporting summaries, source data, extended data, supplementary information, acknowledgements, peer review information; details of author contributions and competing interests; and statements of data and code availability are available at https://doi.org/10.1038/s41586-022-05399-1.

1. Pinaud, B. A. et al. Technical and economic feasibility of centralized facilities for solar hydrogen production via photocatalysis and photoelectrochemistry. *Energy Environ. Sci.* **6**, 1983–2002 (2013).
2. Hisatomi, T. & Domen, K. Reaction systems for solar hydrogen production via water splitting with particulate semiconductor photocatalysts. *Nat. Catal.* **2**, 387–399 (2019).
3. Rodriguez, C. A., Modestino, M. A., Psaltis, D. & Moser, C. Design and cost considerations for practical solar-hydrogen generators. *Energy Environ. Sci.* **7**, 3828–3835 (2014).
4. Goto, Y. et al. A particulate photocatalyst water-splitting panel for large-scale solar hydrogen generation. *Joule* **2**, 509–520 (2018).
5. Guan, X. et al. Efficient unassisted overall photocatalytic seawater splitting on GaN-based nanowire arrays. *J. Phys. Chem. C* **122**, 13797–13802 (2018).
6. Ager, J. W., Shaner, M. R., Walczak, K. A., Sharp, I. D. & Ardo, S. Experimental demonstrations of spontaneous, solar-driven photoelectrochemical water splitting. *Energy Environ. Sci.* **8**, 2811–2824 (2015).
7. Khaselev, O. & Turner, J. A. A monolithic photovoltaic-photoelectrochemical device for hydrogen production via water splitting. *Science* **280**, 425–427 (1998).
8. Kang, D. et al. Printed assemblies of GaAs photoelectrodes with decoupled optical and reactive interfaces for unassisted solar water splitting. *Nat. Energy* **2**, 17043 (2017).
9. Chowdhury, F. A., Trudeau, M. L., Guo, H. & Mi, Z. A photochemical diode artificial photosynthesis system for unassisted high efficiency overall pure water splitting. *Nat. Commun.* **9**, 1707 (2018).
10. Wang, Q. et al. Scalable water splitting on particulate photocatalyst sheets with a solar-to-hydrogen energy conversion efficiency exceeding 1%. *Nat. Mater.* **15**, 611–615 (2016).
11. Maeda, K. et al. Noble-metal/Cr₂O₃ core/shell nanoparticles as a cocatalyst for photocatalytic overall water Splitting. *Angew. Chem. Int. Edn* **45**, 7806–7809 (2006).
12. Takata, T. et al. Photocatalytic water splitting with a quantum efficiency of almost unity. *Nature* **581**, 411–414 (2020).
13. Fountaine, K. T., Lewerenz, H. J. & Atwater, H. A. Efficiency limits for photoelectrochemical water-splitting. *Nat. Commun.* **7**, 13706 (2016).
14. Kibria, M. G. et al. Visible light-driven efficient overall water splitting using p-type metal-nitride nanowire arrays. *Nat. Commun.* **6**, 6797 (2015).
15. Licht, S. Solar water splitting to generate hydrogen fuel: photothermal electrochemical analysis. *J. Phys. Chem. B* **107**, 4253–4260 (2003).
16. Moses, P. G. & Walle, C. G. V. D. Band bowing and band alignment in InGaN alloys. *Appl. Phys. Lett.* **96**, 021908 (2010).
17. Wang, Y., Wu, Y., Sun, K. & Mi, Z. A quadruple-band metal–nitride nanowire artificial photosynthesis system for high efficiency photocatalytic overall solar water splitting. *Mater. Horiz.* **6**, 1454–1462 (2019).
18. Kibria, M. G. et al. Tuning the surface Fermi level on p-type gallium nitride nanowires for efficient overall water splitting. *Nat. Commun.* **5**, 3825 (2014).
19. Guan, X. et al. Making of an industry-friendly artificial photosynthesis device. *ACS Energy Lett.* **3**, 2230–2231 (2018).
20. Xu, Y. & Schoonen, M. A. A. The absolute energy positions of conduction and valence bands of selected semiconducting minerals. *Am. Mineral.* **85**, 543–556 (2000).
21. Zhou, P., Yu, J. & Jaroniec, M. All-solid-state Z-scheme photocatalytic systems. *Adv. Mater.* **26**, 4920–4935 (2014).
22. Nishiyama, H. et al. Photocatalytic solar hydrogen production from water on a 100-m² scale. *Nature* **598**, 304–307 (2021).
23. Zhang, B., Daniel, Q., Cheng, M., Fan, L. & Sun, L. Temperature dependence of electrocatalytic water oxidation: a triple device model with a photothermal collector and photovoltaic cell coupled to an electrolyzer. *Faraday Discuss.* **198**, 169–179 (2017).
24. Jin, B. et al. Promoting oxygen evolution reaction of Co-based catalysts (Co₃O₄, CoS, CoP, and CoN) through photothermal effect. *Small* **15**, 1903847 (2019).
25. Tembhurne, S., Nandjou, F. & Haussener, S. A thermally synergistic photo-electrochemical hydrogen generator operating under concentrated solar irradiation. *Nat. Energy* **4**, 399–407 (2019).
26. Seh, Z. W. et al. Combining theory and experiment in electrocatalysis: insights into materials design. *Science* **355**, eaad4998 (2017).
27. Zhang, Y. et al. Rate-limiting O–O bond formation pathways for water oxidation on hematite photoanode. *J. Am. Chem. Soc.* **140**, 3264–3269 (2018).
28. Hisatomi, T., Takanabe, K. & Domen, K. Photocatalytic water-splitting reaction from catalytic and kinetic perspectives. *Catal. Lett.* **145**, 95–108 (2015).
29. Wang, M., Zhen, W., Tian, B., Ma, J. & Lu, G. The inhibition of hydrogen and oxygen recombination reaction by halogen atoms on over-all water splitting over Pt–TiO₂ photocatalyst. *Appl. Catal. B* **236**, 240–252 (2018).
30. Wang, M., Li, Z., Wu, Y., Ma, J. & Lu, G. Inhibition of hydrogen and oxygen reverse recombination reaction over Pt/TiO₂ by F⁻ ions and its impact on the photocatalytic hydrogen formation. *J. Catal.* **353**, 162–170 (2017).
31. Zhang, Y., Hu, H., Huang, X. & Bi, Y. Photo-controlled bond changes on Pt/TiO₂ for promoting overall water splitting and restraining hydrogen–oxygen recombination. *J. Mater. Chem. A* **7**, 5938–5942 (2019).
32. Verhallen, P. T. H. M., Oomen, L. J. P., Elsen, A. J. J. M. V. D., Kruger, J. & Fortuin, J. M. H. The diffusion coefficients of helium, hydrogen, oxygen and nitrogen in water determined from the permeability of a stagnant liquid layer in the quasi-steady state. *Chem. Eng. Sci.* **39**, 1535–1541 (1984).
33. Nguyen, H. P. T., Djavid, M., Cui, K. & Mi, Z. Temperature-dependent nonradiative recombination processes in GaN-based nanowire white-light-emitting diodes on silicon. *Nanotechnology* **23**, 194012 (2012).

Methods

Synthesis of InGaN/GaN NWs

InGaN/GaN NWs were grown on a three-inch silicon wafer by molecular-beam-epitaxy technology[34,35], which have also been widely grown utilizing various other processes, such as chemical vapour deposition and sputtering[36,37]. The silicon wafer was first cleaned with acetone and 10% buffered hydrofluoric acid. Then the residual oxide on the silicon wafer was removed by in situ annealing at about 787 °C in the reaction chamber before growth. The InGaN/GaN NWs were spontaneously grown on the silicon wafer under nitrogen-rich conditions to promote the formation of nitrogen-rich surfaces to prevent photo-corrosion and oxidation. Gallium (Ga), In and magnesium fluxes were controlled by using thermal effusion cells, while nitrogen radicals were produced from a radio-frequency nitrogen plasma source. Multi-stack InGaN/GaN layers were grown on a GaN layer and finally terminated by a GaN capping layer. A nitrogen flow rate of 1.0 standard cubic centimetres per minute and a forward plasma power of about 350 W were used in the growth process.

Cocatalyst loading

Rh/Cr$_2$O$_3$ core/shell and Co$_3$O$_4$ nanoparticles were loaded on InGaN/GaN NWs by a typical in situ photodeposition[38,39]. In a detailed process, a 0.8 cm × 0.8 cm photocatalyst wafer was first stabilized on a Teflon holder. Then the holder was transferred to the 390-ml chamber containing 50 ml of 20 vol% methanol aqueous solution. Then 5 μl of 0.2 mol l^{-1} Na$_3$RhCl$_6$ (Sigma-Aldrich) was added into the methanol aqueous solution. The chamber was covered by a quartz cover and vacuumized. After that, the chamber was irradiated under a 300-W Xe lamp (Cermax, PE300BUV) for 10 min. After reaction, 5 μl of 0.2 mol l^{-1} K$_2$CrO$_4$ (Sigma-Aldrich) was injected into the chamber and the chamber was irradiated for another 10 min. Similarly, 5 μl of 0.2 mol l^{-1} Co(NO$_3$)$_2$·6H$_2$O (Sigma-Aldrich) was also injected into the chamber and then irradiated for 20 min. Finally, the obtained photocatalyst wafer was washed by deionized water and dried at 80 °C in air. It is noted that the deposited metallic cobalt (Co) nanoparticles in photoreduction can be readily oxidized in air, which were finally converted into Co$_3$O$_4$ nanoparticles. The photocatalyst wafers with different cocatalyst contents were also prepared by changing the precursors. For the outdoor test, Rh/Cr$_2$O$_3$ core/shell and Co$_3$O$_4$ nanoparticles were loaded on the 4 cm × 4 cm photocatalyst wafer by using 125 μl of 0.2 mol l^{-1} Na$_3$RhCl$_6$, 125 μl of 0.2 mol l^{-1} K$_2$CrO$_4$ and 125 μl of 0.2 mol l^{-1} Co(NO$_3$)$_2$·6H$_2$O in the photodeposition. Other procedures were the same as described above.

Characterization

The crystal structure of InGaN/GaN NWs was examined by XRD, which was collected on a Rigaku X-ray diffractometer equipped with Cu Kα radiation working at an acceleration voltage of 40 kV and a current of 80 mA. The scanning rate was set to 0.05° 2θ s^{-1} (θ, angle). The morphology of the samples was observed using a Hitachi SU8000 FESEM at an acceleration voltage of 10 kV. The HRTEM and HAADF-STEM analyses were performed on a JEOL 3100R05 double spherical aberration corrected TEM/STEM with a 300-kV acceleration voltage. The ultraviolet–visible diffuse reflectance spectrum was collected using a Shimadzu UV-2600 spectrophotometer. The various bandgaps of the InGaN structures were attributed to the different In distributions according to Vegard's law[40–42], which improved the utilization efficiency of visible light[43–46]. The band-edge potentials were calculated according to the reported formula[20]:

$$E_{CB} = \chi + E_0 - 0.5E_g$$

where E_{CB}, χ and E_g are the conduction band-edge potential, absolute electronegativity of pristine InGaN and bandgap of InGaN, respectively. E_0 is a constant (−4.5 eV) that stands for the Fermi level of the normal hydrogen electrode at 25 °C with respect to the vacuum level. The valence band-edge potential (E_{VB}) can be directly calculated by the following formula:

$$E_{VB} = E_{CB} - E_g$$

The SEM-CL measurements were conducted on a Tescan Rise scanning electron microscope with an acceleration voltage of 10 kV.

Photocatalytic OWS

Photocatalytic OWS was performed in a 390-ml Pyrex chamber containing 50 ml deionized water under a 300-W Xe lamp equipped with an AM1.5G filter. The 0.8 cm × 0.8 cm photocatalyst wafer loaded with Rh/Cr$_2$O$_3$ core/shell and Co$_3$O$_4$ nanoparticles was stabilized in the holder with a volume of 10 ml. The holder was installed on the bottom of the Pyrex chamber, and covered by a vacuum-tight quartz lid and a vacuum-tight plastic ring. Before the photocatalytic reaction, the chamber was vacuumized to a reduced pressure, which helps reduce the back reaction and to enhance the extraction of hydrogen and oxygen produced in the reaction. A vacuum-tight plastic ring connected the chamber with vacuum-tight quartz lid. The light intensity on the photocatalyst wafer was measured to be 3,800 mW cm^{-2} by a thermopile detector (919P, Newport Corporation). A circulating water layer or heat-insulating layer was used to control the temperature of the chamber under continuous light irradiation (Extended Data Figs. 3 and 4), and to maintain the reaction chamber at a stable temperature. At the start of the experiment, only water vapour existed in the gas phase of the chamber. With hydrogen and oxygen production, the pressure in the chamber increased with reaction time (Extended Data Table 2). The produced hydrogen and oxygen were manually sampled each hour by using a vacuum-tight syringe, and analysed in a gas chromatograph (Shimadzu GC-8A) equipped with a thermal conductivity detector and a 5-Å molecular-sieve column. The thermal conductivity detector and the 5-Å molecular-sieve column using high-purity argon as the carrier gas worked at 110 °C and 50 °C, respectively. In the stability test of the photocatalyst, the chamber was repeatedly vacuumized each hour to exclude the hydrogen and oxygen produced in the last cycle before the next cycle.

For the large-scale outdoor experiments under natural solar light[47], a 4 cm × 4 cm photocatalyst wafer was stabilized on a holder with a volume of about 50 ml. The photocatalyst wafer and holder were installed in a well designed chamber with a volume of 4,350 ml containing 300 ml deionized water. In general, the use of concentrated sunlight, as shown in recent studies, can significantly reduce the cost of solar hydrogen production[3,48–51]. Thus, a 1.1 m × 1.1 m Fresnel lens was used to produce concentrated solar light of about 16,070 mW cm^{-2} on an approximately 8 cm × 8 cm plane region in which the as-prepared 4 cm × 4 cm photocatalyst wafer was installed (Extended Data Fig. 8). The sampling, analysing and circling procedures were the same as described above for the indoor testing. In the stability test, the chamber was repeatedly vacuumized every 10 min to exclude the produced hydrogen and oxygen before the next cycle.

Calculation of STH efficiency

The STH efficiency of the photocatalytic OWS devices was calculated by the following formula[52–56]:

$$\begin{aligned} STH = &\text{Hydrogen production rate (mmol s}^{-1}) \\ &\times 237,000 \text{ J mol}^{-1}/\text{Light intensity (mW cm}^{-2}) \quad (1) \\ &/\text{Wafer area (cm}^2) \end{aligned}$$

where 237,000 J mol^{-1} is the reaction Gibbs free energy of OWS.

The theoretical maximum STH conversion efficiency for a photocatalyst system absorbing photons with wavelengths (λ, nm) up to λ_{max} (nm) was calculated by the following formulas:

Article

$$\text{Number of photons } (s^{-1}\,m^{-2}, \lambda < \lambda_{max})$$
$$= \int_{280nm}^{\lambda\,max} \text{Light power density } (Wm^{-2}\,nm^{-1}) \tag{2}$$
$$\times \lambda(nm)/1,240\,eV\,nm/(1.6\times10^{-19}\,J)\,d\lambda\,(nm)$$

where 1,240 (eV nm) is the coefficient of wavelength-to-energy conversion and 1.6×10^{-19} (J) is the energy of 1 eV.

$$\text{Amount of H}_2 \text{ molecules } (mol\,s^{-1}\,m^{-2})$$
$$= \text{Number of photons } (s^{-1}\,m^{-2}, \lambda < \lambda_{max})/2/(6.02\times10^{23}\,mol^{-1}) \tag{3}$$

$$\text{STH}_{max}\,(\%) = \text{Amount of H}_2 \text{ molecules } (mol\,s^{-1}\,m^{-2})$$
$$\times 237,000\,J\,mol^{-1}/\text{Light intensity } (J\,s^{-1}\,m^{-2})\times100\% \tag{4}$$

The obtained results are shown in Extended Data Fig. 2.

Calculation of TON and TOF

The TON and TOF for OWS were calculated by the following formula:

$$\text{TON} = \text{Hydrogen production amount (mmol)} \\ /\text{Photocatalyst amount (mmol)} \tag{5}$$

$$\text{TOF} = \text{Hydrogen production amount (mmol)} \\ /\text{Photocatalyst amount (mmol)} \\ /\text{Reaction time (h)} \tag{6}$$

The mass density of Ga(In)N on silicon wafer was $6.15\,g\,cm^{-3}$. The amount of photocatalyst on $0.64\,cm^{-2}$ of silicon wafer used in the photocatalytic OWS was calculated to be 5.64 µmol.

Theoretical simulation

The hydrogen–oxygen recombination reaction on the cocatalyst Co_3O_4, Rh and Cr_2O_3 was studied by DFT calculations based on the Vienna Ab initio Simulation Package. The revised Perdew–Burke–Ernzerhof exchange-correlation function of the generalized gradient approximation was adopted in all calculations. The interaction between valence electrons and the ionic core was described with the projector augmented wave pseudo-potential. The Co_3O_4, Rh and Cr_2O_3 surfaces were simulated by their typical Co_3O_4 (311), Rh (111) and Cr_2O_3 (104) facets, respectively. A $1\times2\,Co_3O_4$ (311) supercell with three O–Co–O layers, a 3×4 Rh (111) supercell with four Rh layers and a $2\times2\,Cr_2O_3$ (104) supercell with three O–Cr–O layers were used in the simulation. The geometry optimization was conducted with the convergence threshold of $0.001\,eV\,Å^{-1}$ and a cut-off of 400 eV at the Γ point.

Data availability

Supporting data are available at the University of Michigan (https://doi.org/10.7302/g0xw-d923). Further details regarding the data are available from the corresponding author upon reasonable request.

34. Kibria, M. G. et al. One-step overall water splitting under visible light using multiband InGaN/GaN nanowire heterostructures. *ACS Nano* **7**, 7886–7893 (2013).

35. Kibria, M. G. & Mi, Z. Artificial photosynthesis using metal/nonmetal-nitride semiconductors: current status, prospects, and challenges. *J. Mater. Chem. A* **4**, 2801–2820 (2016).
36. Benton, J., Bai, J. & Wang, T. Utilisation of GaN and InGaN/GaN with nanoporous structures for water splitting. *Appl. Phys. Lett.* **105**, 223902 (2014).
37. Aryal, K., Pantha, B. N., Li, J., Lin, J. Y. & Jiang, H. X. Hydrogen generation by solar water splitting using p-InGaN photoelectrochemical cells. *Appl. Phys. Lett.* **96**, 052110 (2010).
38. Fabian, D. M. et al. Particle suspension reactors and materials for solar-driven water splitting. *Energy Environ. Sci.* **8**, 2825–2850 (2015).
39. Hisatomi, T., Kubota, J. & Domen, K. Recent advances in semiconductors for photocatalytic and photoelectrochemical water splitting. *Chem. Soc. Rev.* **43**, 7520–7535 (2014).
40. Pelá, R. R. et al. Accurate band gaps of AlGaN, InGaN, and AlInN alloys calculations based on LDA-1/2 approach. *Appl. Phys. Lett.* **98**, 151907 (2011).
41. Vurgaftman, I., Meyer, J. R. & Ram-Mohan, L. R. Band parameters for III–V compound semiconductors and their alloys. *J. Appl. Phys.* **89**, 5815–5875 (2001).
42. Kuykendall, T., Ulrich, P., Aloni, S. & Yang, P. Complete composition tunability of InGaN nanowires using a combinatorial approach. *Nat. Mater.* **6**, 951–956 (2007).
43. Young, J. L. et al. Direct solar-to-hydrogen conversion via inverted metamorphic multi-junction semiconductor architectures. *Nat. Energy* **2**, 17028 (2017).
44. Cheng, W.-H. et al. Monolithic photoelectrochemical device for direct water splitting with 19% efficiency. *ACS Energy Lett.* **3**, 1795–1800 (2018).
45. Li, X. et al. Engineering heterogeneous semiconductors for solar water splitting. *J. Mater. Chem. A* **3**, 2485–2534 (2015).
46. Zou, Z., Ye, J., Sayama, K. & Arakawa, H. Direct splitting of water under visible light irradiation with an oxide semiconductor photocatalyst. *Nature* **414**, 625–627 (2001).
47. Diffey, B. Solar spectral irradiance and summary outputs using excel. *Photochem. Photobiol.* **91**, 553–557 (2015).
48. Shaner, M. R., Atwater, H. A., Lewis, N. S. & McFarland, E. W. A comparative technoeconomic analysis of renewable hydrogen production using solar energy. *Energy Environ. Sci.* **9**, 2354–2371 (2016).
49. Kim, J. H., Hansora, D., Sharma, P., Jang, J.-W. & Lee, J. S. Toward practical solar hydrogen production – an artificial photosynthetic leaf-to-farm challenge. *Chem. Soc. Rev.* **48**, 1908–1971 (2019).
50. Lewis, N. S. Research opportunities to advance solar energy utilization. *Science* **351**, aad1920 (2016).
51. Tachibana, Y., Vayssieres, L. & Durrant, J. R. Artificial photosynthesis for solar water-splitting. *Nat. Photon.* **6**, 511–518 (2012).
52. Liao, L. B. et al. Efficient solar water-splitting using a nanocrystalline CoO photocatalyst. *Nat. Nanotechnol.* **9**, 69–73 (2014).
53. Kim, J. H. et al. Wireless solar water splitting device with robust cobalt-catalyzed, dual-doped BiVO₄ photoanode and perovskite solar cell in tandem: a dual absorber artificial leaf. *ACS Nano* **9**, 11820–11829 (2015).
54. Liu, W. et al. Single-site active cobalt-based photocatalyst with a long carrier lifetime for spontaneous overall water splitting. *Angew. Chem. Int. Edn* **56**, 9312–9317 (2017).
55. Liu, C., Tang, J., Chen, H. M., Liu, B. & Yang, P. A fully integrated nanosystem of semiconductor nanowires for direct solar water splitting. *Nano Lett.* **13**, 2989–2992 (2013).
56. Wang, Q. et al. Oxysulfide photocatalyst for visible-light-driven overall water splitting. *Nat. Mater.* **18**, 827–832 (2019).

Author contributions P.Z. designed the photocatalyst and performed the photocatalytic reactions. I.A.N. synthesized the InGaN/GaN NWs. Y.X., K.S. and P.W. performed SEM and TEM. P.Z., Y.M., B.Z. and Z.Y. performed the outdoor photocatalytic experiments. Z.M. supervised the whole project. P.Z. and Z.M. wrote the manuscript with input from all authors.
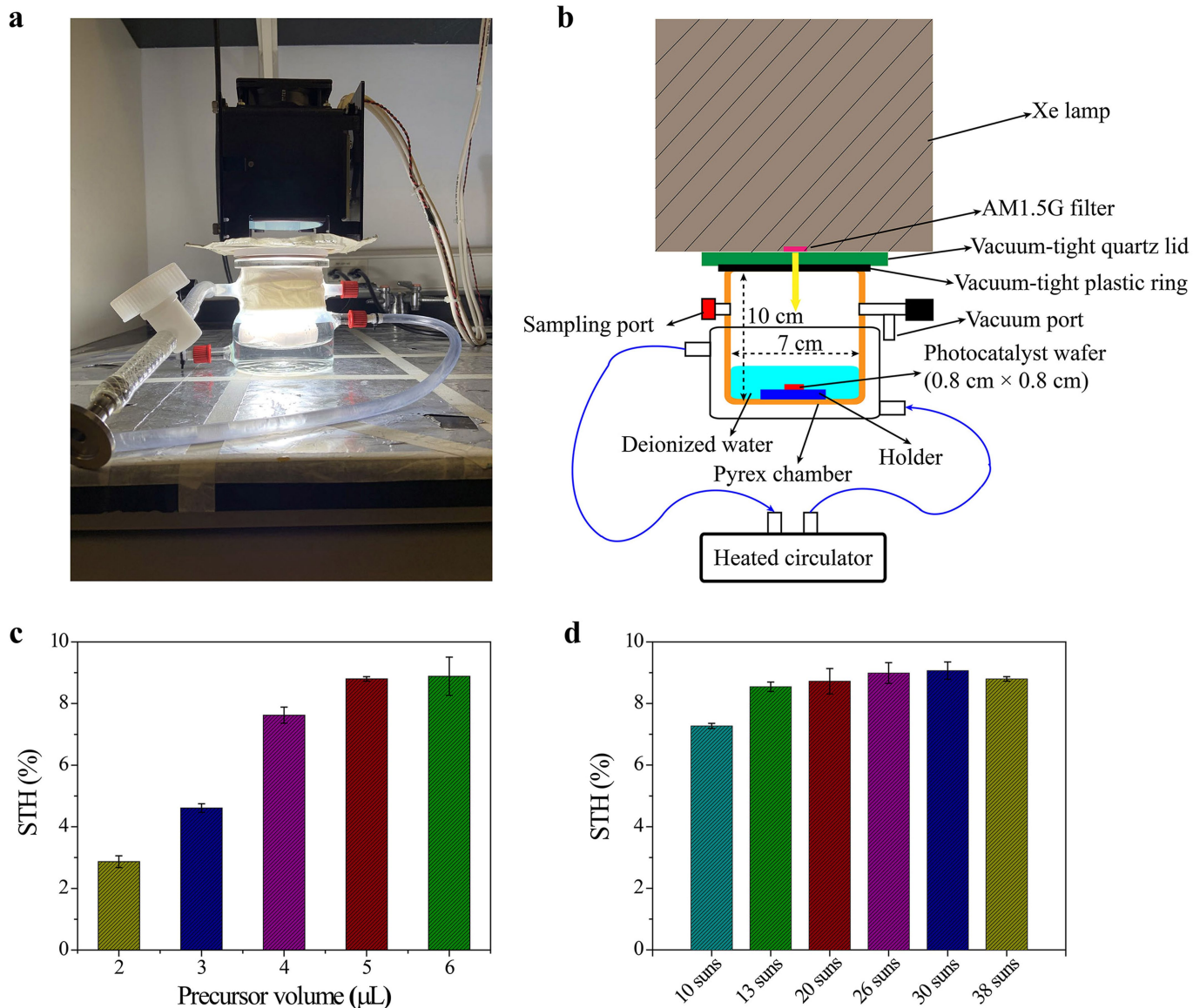
Extended Data Fig. 1 | Bandgap determination. SEM-CL images of InGaN/GaN nanowires. The high-energy electrons from the scanning electron microscope were used to photo-excite photocatalyst to produce photogenerated electrons and holes. The recombination of photogenerated electrons and holes leads to the cathodoluminescence phenomenon, which could be used to estimate the bandgap of the photocatalyst. A bandwidth of 5 nm was used to capture these monochromatic CL images. The luminescence bands at 445–545 nm revealed the visible-light response of InGaN/GaN nanowires.

a

b

c

d
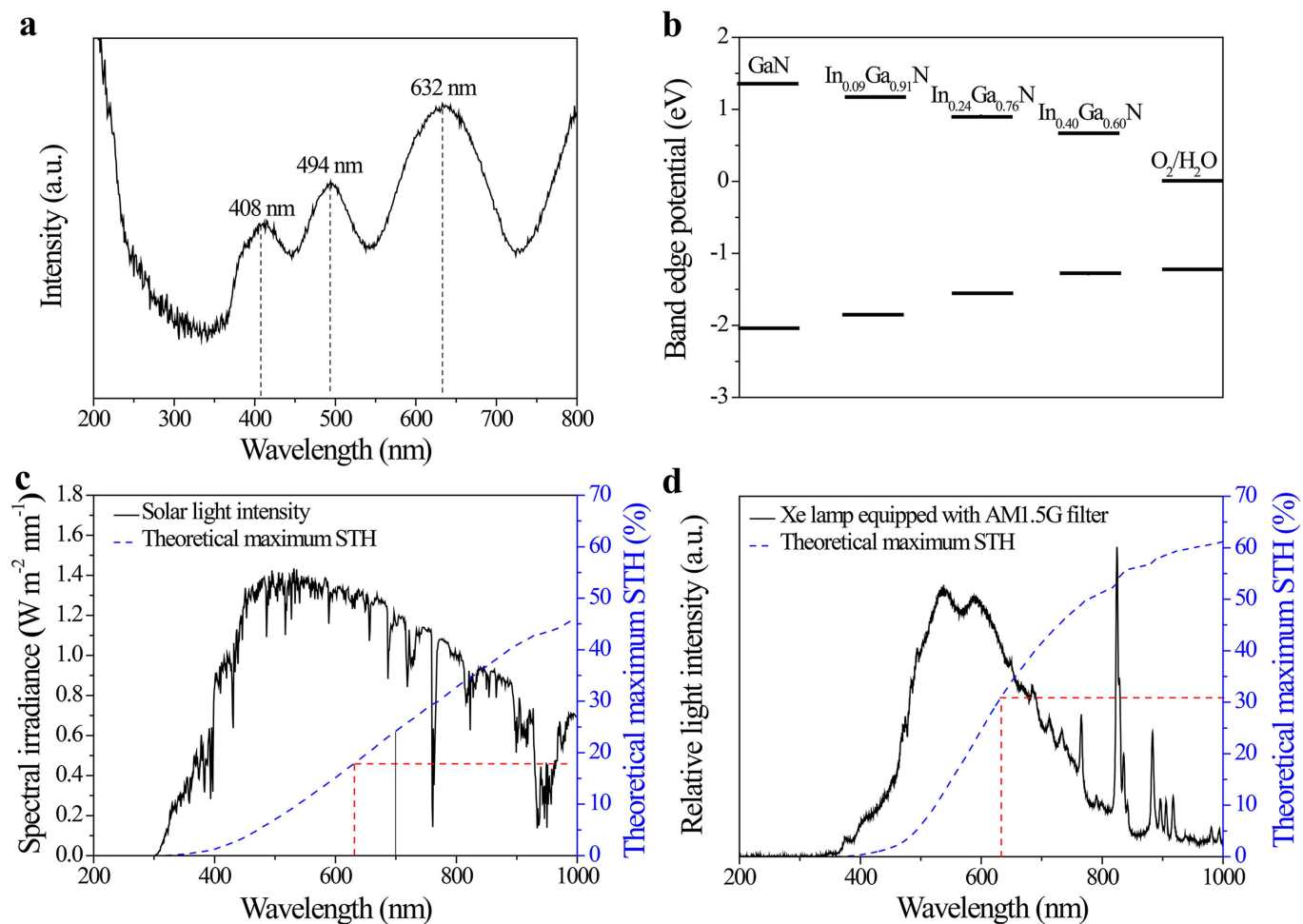
Extended Data Fig. 2 | Light-response characterization and theoretical maximum STH. a, UV-vis diffuse reflectance spectroscopy of InGaN/GaN suggests that the visible-light-response range of InGaN/GaN nanostructures is extended to 632 nm (1.96 eV). **b**, Band diagram of InGaN/GaN segments.

c, **d**, Wavelength-dependent theoretical maximum STH in (**c**) natural solar light and (**d**) simulated solar light produced by a Xe lamp equipped with a standard AM1.5G filter from Newport Corporation. The red dashed line corresponds to a photocatalyst with bandgap of 1.96 eV (632 nm).

a

b

Xe lamp

AM1.5G filter

Vacuum-tight quartz lid

Vacuum-tight plastic ring

Sampling port

10 cm

7 cm

Vacuum port

Photocatalyst wafer
(0.8 cm × 0.8 cm)

Deionized water

Holder

Pyrex chamber

Heated circulator

c

STH (%)

Precursor volume (μL)

d

STH (%)

10 suns 13 suns 20 suns 26 suns 30 suns 38 suns

Extended Data Fig. 3 | Temperature-controllable photocatalytic OWS system and reaction condition optimization. a, Temperature-controllable photocatalytic OWS system. **b**, Schematic illustration of the temperature-controllable photocatalytic OWS system. A double-layer chamber was used to perform the temperature-controllable photocatalytic OWS. The circulating water provided by a PolyScience 7L heated circulator was used to control the temperature of the reaction chamber. **c**, STH of InGaN/GaN NWs with different $Rh/Cr_2O_3/Co_3O_4$ precursor volumes at 70 °C. x ($x = 2, 3, 4, 5, 6$) μl of 0.2 mol l^{-1} Na_3RhCl_6, x μl of 0.2 mol l^{-1} K_2CrO_4, x μl of 0.2 mol l^{-1} $Co(NO_3)_2·6H_2O$ were used in the photodeposition of cocatalyst. The photodeposition method was shown in the experimental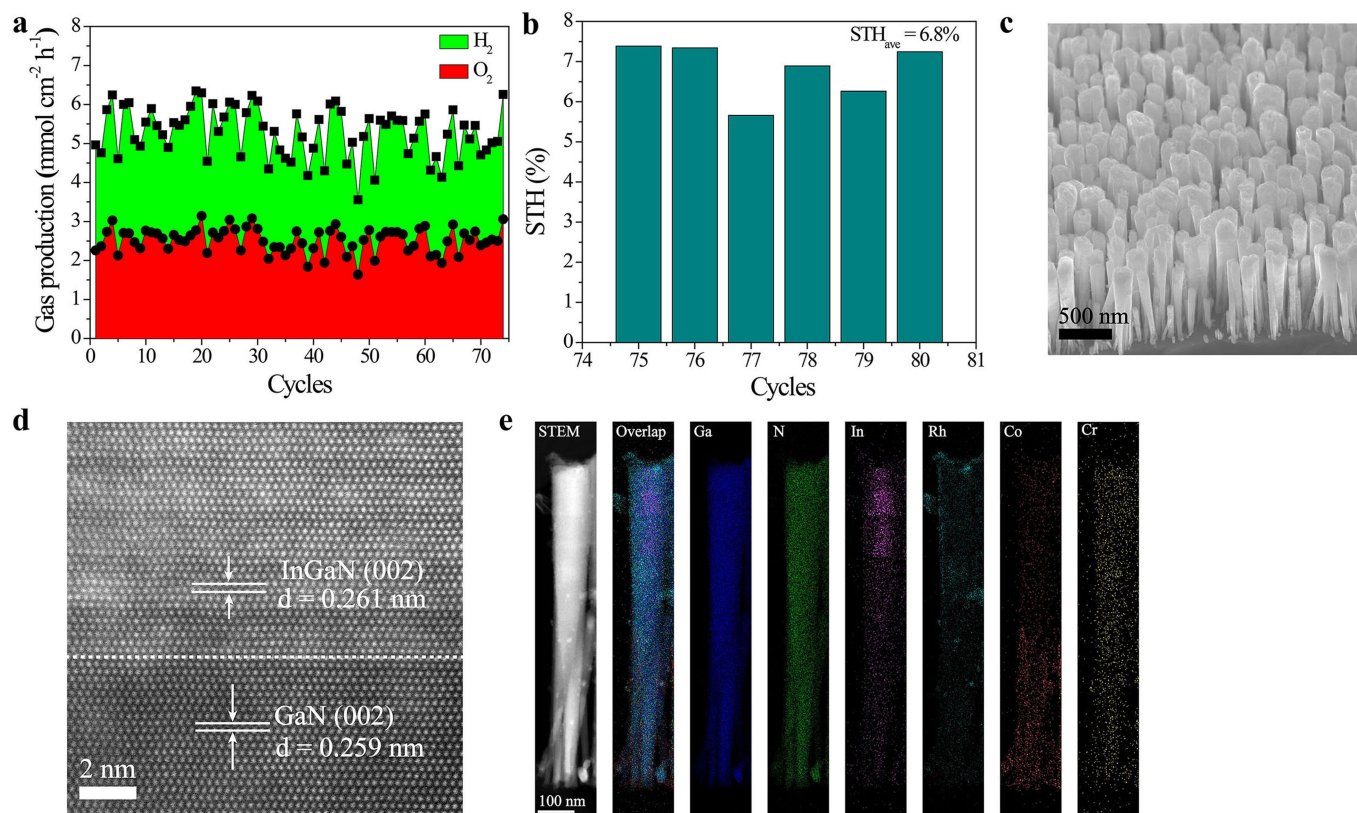 section. The optimized contents (μg cm^{-2}) of cocatalyst obtained by ICP was shown in the Extended Data Table 1. **d**, STH of $Rh/Cr_2O_3/Co_3O_4$-InGaN/GaN NWs under different light intensity at 70 °C. 1 sun: 100 mW cm^{-2}. The STH of $Rh/Cr_2O_3/Co_3O_4$-InGaN/GaN NWs first increased with cocatalyst content and then reached a maximum value. A further increase on the cocatalyst content could not improve the STH. The optimized cocatalyst content was utilized in all subsequent experiments. The light intensity on the photocatalyst wafer was adjusted from 1,000 mW cm^{-2} to 3,800 mW cm^{-2} at 70 °C. The results showed that the STH was not observably changed with the light intensity larger than 13 suns at the same temperature (70 °C). Error bars indicate standard deviation for three measurements.
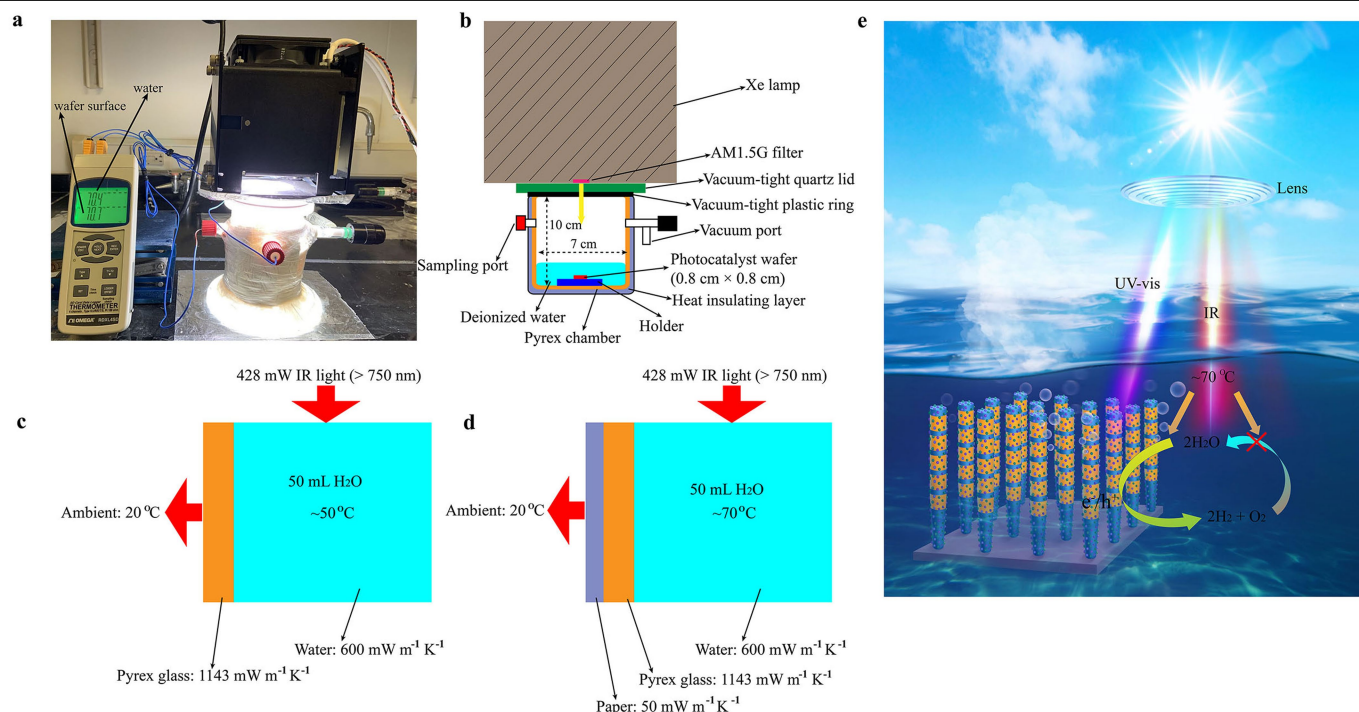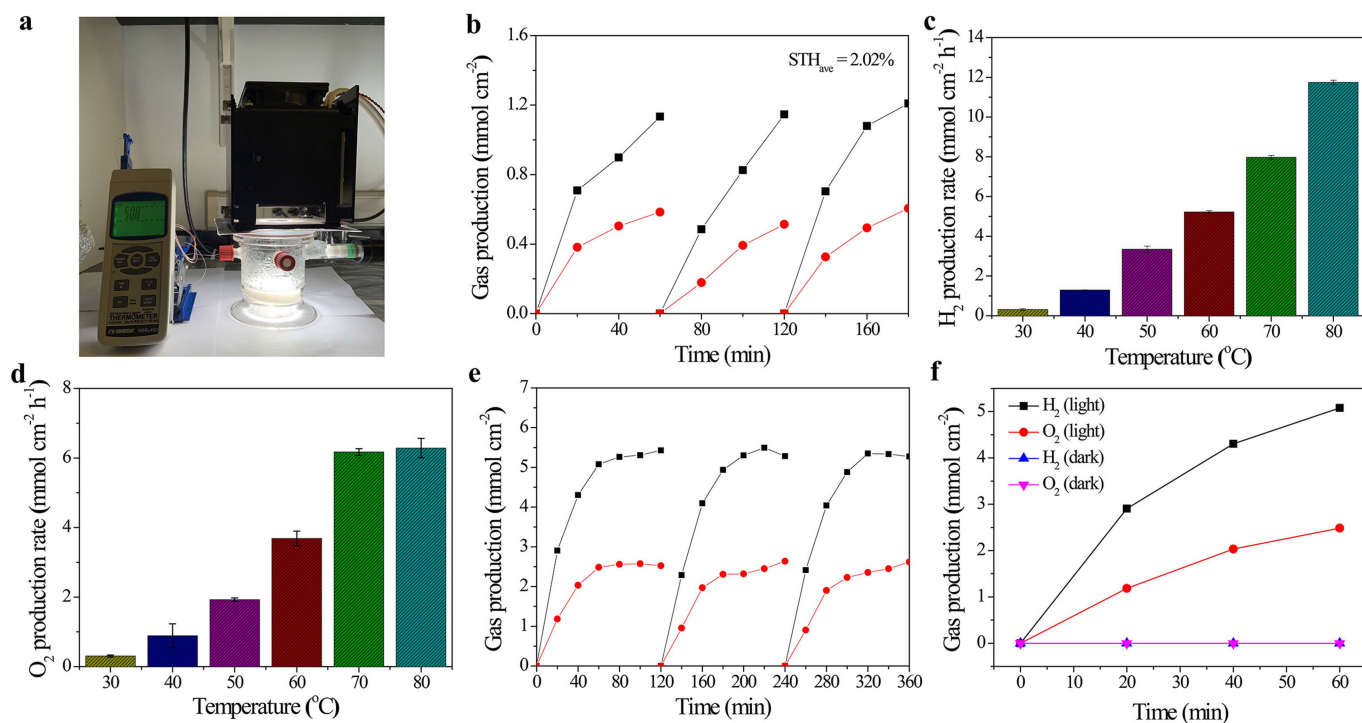
Extended Data Fig. 4 | Self-heated photocatalytic OWS system. a, Self-heated photocatalytic OWS system. **b**, Schematic parameters of the self-heated photocatalytic OWS system. **c**, **d**, Thermodynamic parameters of the reaction system (**c**) without and (**d**) with a heat-insulating layer. The heat-insulating layer (thickness of approximately 0.5 cm) consisted of ordinary A4 printing paper. The wall thickness of the Prexy chamber was approximately 0.3 cm. **e**, Synergetic effect mechanism of promoting forward hydrogen–oxygen evolution and inhibiting the reverse hydrogen–oxygen recombination in the photocatalytic OWS. The UV-vis light was responsible for the production of photogenerated electrons and holes via the photoexcitation of InGaN/GaN semiconductor, which can further cause the redox of water. Although the infrared light was non-effective for the photoexcitation of InGaN/GaN, it could produce a substantial thermal effect to promote hydrogen/oxygen production and simultaneously inhibit the hydrogen–oxygen recombination. In this mechanism, the infrared light indirectly, but substantially improved the utilization efficiency of UV-vis

light by enhancing the surface catalytic hydrogen/oxygen production, which finally contributed to the maximizing of STH. A thermal transfer balance existed in our system during photocatalytic reaction, which was influenced by the thermal conductivity coefficients of materials used in the reaction system. The role of the heat-insulating layer was to produce a larger temperature difference between ambient and internal environment of reaction system. The thermal conductivity coefficients of Prexy glass, heat-insulating layer and water were 1,143, 50 and 600 mW m^{-1} K^{-1}, respectively. In the absence of the heat-insulating layer, the temperature of water in the chamber was maintained at roughly 50 °C. However, with the addition of low thermal-conductivity heat-insulating layer, the temperature of reaction system could be increased to approximately 70 °C under the same IR input (428 mW). The species and content of impurities in tap water can be found on the website of Ann Arbor Water Treatment Services Unit (https://www.a2gov.org/departments/water-treatment/Documents/water_quality_report_2020.pdf).

a, Time-course photocatalytic production of H_2 and O_2 in deionized water on Rh/Cr$_2$O$_3$/Co$_3$O$_4$-InGaN/GaN NWs. **b**, Activity test after 74-hour photocatalytic OWS reaction. **c–e**, FESEM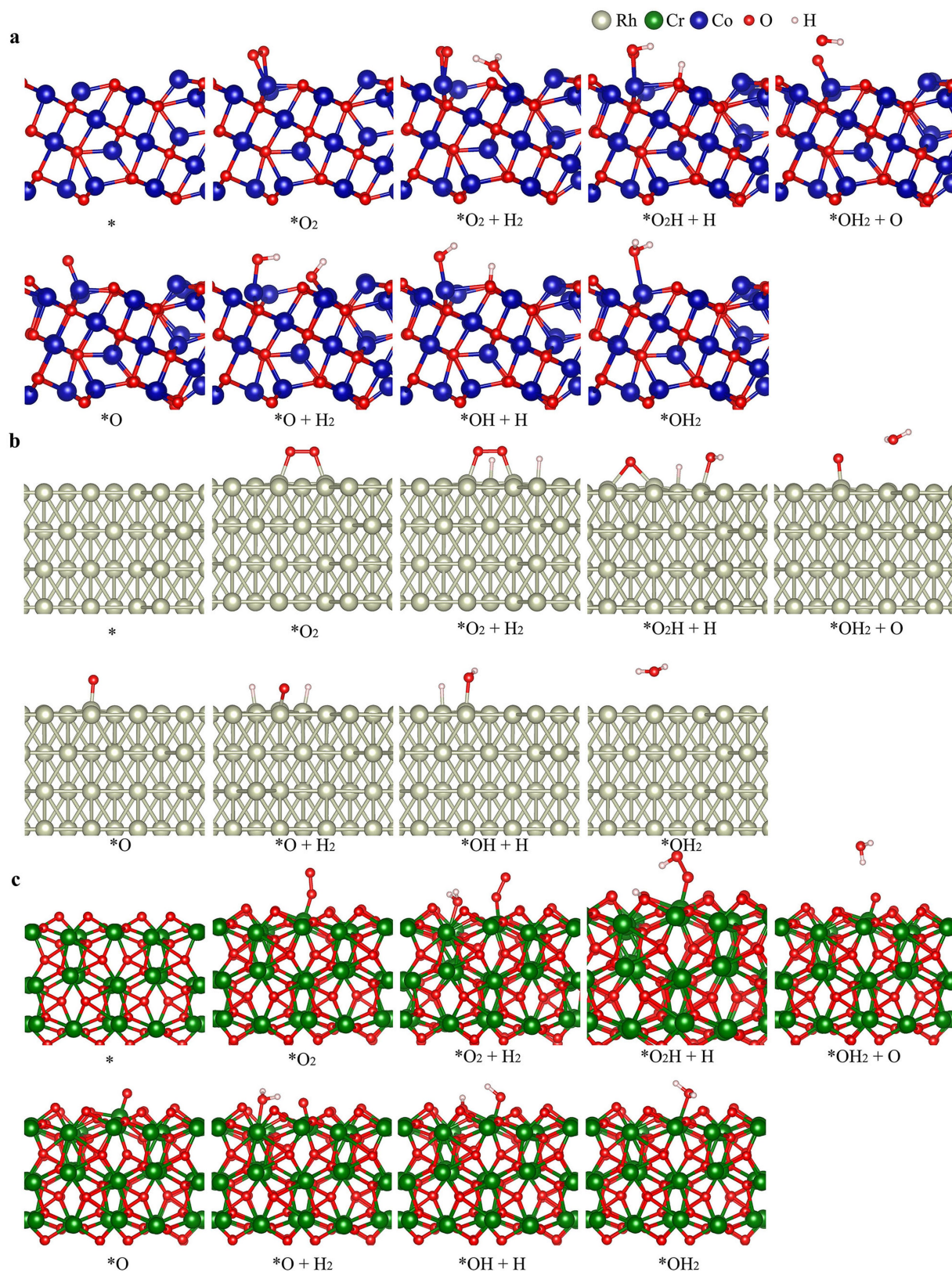 (**c**), HAADF-STEM (**d**) and elemental mapping (**e**) of Rh/Cr$_2$O$_3$/Co$_3$O$_4$-InGaN/GaN NWs after 80-hour photocatalytic OWS reaction.

Extended Data Fig. 5 | Stability evaluation.

Article

Extended Data Fig. 6 | Mechanism investigation of temperature-dependent photocatalytic OWS system. a, Photocatalytic OWS system without circulating water layer or heat-insulating layer. **b**, Corresponding time-course production of stoichiometric H_2 and O_2 in deionized water on $Rh/Cr_2O_3/Co_3O_4$-InGaN/GaN NWs. **c**, Photocatalytic hydrogen production with methanol (20vol%) as electron donor at 70 °C. **d**, Photocatalytic oxygen production with KIO_3 (0.4 mol l⁻¹) as electron acceptor at 70 °C. **e**, Time-course production of stoichiometric H_2 and O_2 in deionized water on $Rh/Cr_2O_3/Co_3O_4$-InGaN/GaN NWs at 70 °C in 360 min. In the photocatalytic overall water splitting, the hydrogen–oxygen production ($2H_2O \rightarrow 2H_2 + O_2$) often competes with hydrogen–oxygen recombination ($2H_2O \leftarrow 2H_2 + O_2$). Commonly, the rate of chemical reaction strongly depends on the concentration of reactant. Thus, in the initial stage of photocatalytic water splitting ($2H_2O \leftrightarrow 2H_2 + O_2$), the reaction rate of hydrogen–oxygen production was theoretically higher than that of hydrogen–oxygen recombination.

However, with increasing hydrogen/oxygen concentration, the hydrogen–oxygen production and recombination would reach a balance. As a result, the amount of produced hydrogen and oxygen could not be further increased with reaction time. Especially, for the continuous flow-type water splitting system, the produced hydrogen and oxygen would be full of chamber under atmospheric pressure before transferred. This easily leads to a high-concentration hydrogen and oxygen in the chamber, which unavoidably leads to the more severe hydrogen–oxygen recombination. **f**, Time-course production of H_2 and O_2 in deionized water on $Rh/Cr_2O_3/Co_3O_4$-InGaN/GaN NWs with and without light source at 70 °C. Light source: 3,800 mW cm⁻² produced by a 300 W Xe lamp equipped with AM1.5G filter. Sample: 0.8 cm × 0.8 cm $Rh/Cr_2O_3/Co_3O_4$-loaded InGaN/GaN nanowires wafer. Error bars indicate standard deviation for three measurements.

Rh ● Cr ● Co ● O ○ H

a

* $*O_2$ $*O_2 + H_2$ $*O_2H + H$ $*OH_2 + O$

$*O$ $*O + H_2$ $*OH + H$ $*OH_2$

b

* $*O_2$ $*O_2 + H_2$ $*O_2H + H$ $*OH_2 + O$

$*O$ $*O + H_2$ $*OH + H$ $*OH_2$

c

* $*O_2$ $*O_2 + H_2$ $*O_2H + H$ $*OH_2 + O$

$*O$ $*O + H_2$ $*OH + H$ $*OH_2$

Extended Data Fig. 7 | Theoretical simulation. a–c, Geometry structures of reaction steps in hydrogen–oxygen recombination on the cocatalyst (**a**) Co_3O_4, (**b**) Rh and (**c**) Cr_2O_3. The results suggested that the desorption of product water was the rate-determining step in hydrogen–oxygen recombination on Co_3O_4 and Cr_2O_3. Besides, this also implied that water tended to be adsorbed on Co_3O_4 and Cr_2O_3, which inhibited the further hydrogen–oxygen adsorption or recombination on them.
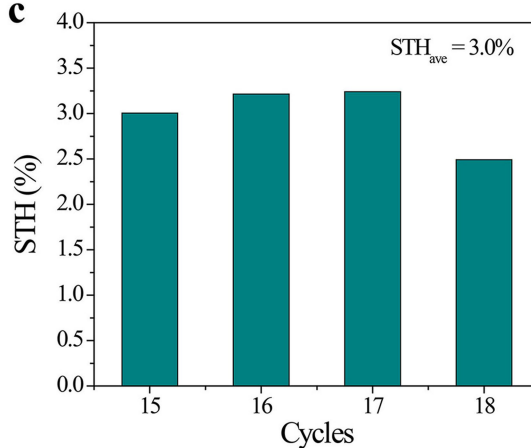
Article

a
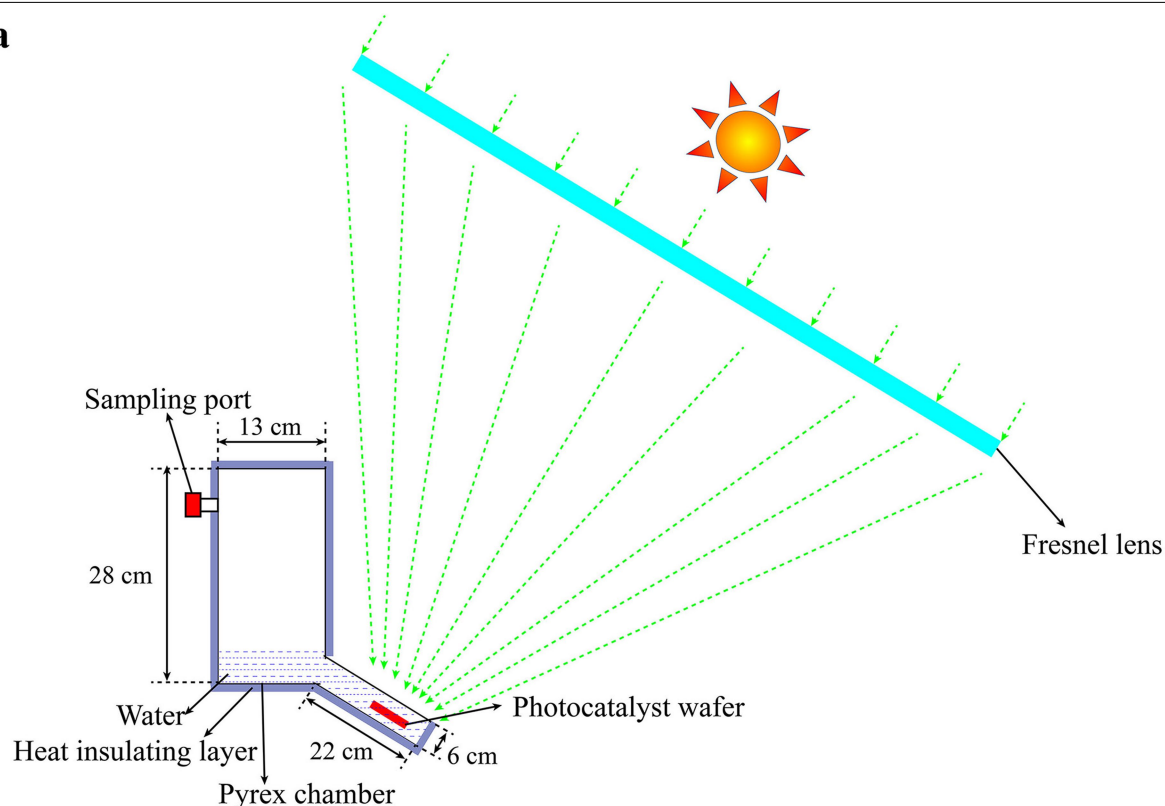
b

c
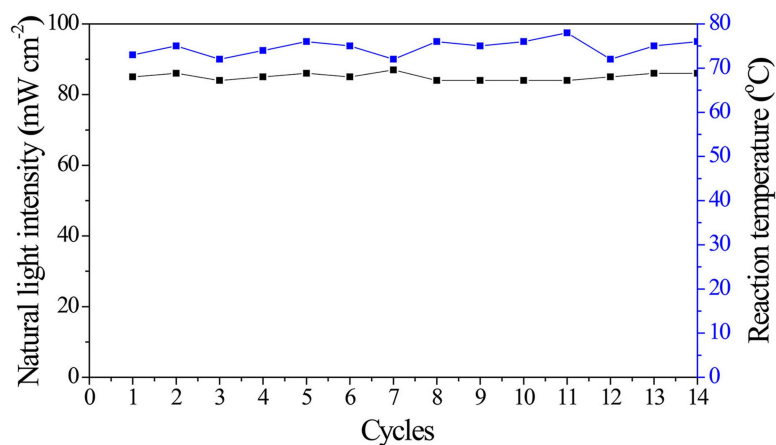
Extended Data Fig. 8 | Photocatalytic OWS under natural concentrated solar light. a, Schematic parameter illustration of outdoor photocatalytic OWS system. **b**, Reaction temperature and natural light intensity in the outdoor test. The thickness of heat-insulating layer (ordinary A4 printing paper) and wall of chamber were approximately 0.5 cm and approximately 0.3 cm, respectively. The outdoor photocatalytic OWS was conducted from 5 November 2020 to 7 November 2020. The average natural solar light intensity was determined to be approximately 85 mW cm^{-2} between 11 pm and 3 pm by a thermopile detector (919P, Newport) with a 5 cm^2 detector. **c**, Activity test after 140-min outdoor photocatalytic OWS reaction. Each cycle: 10 min.

Extended Data Table 1 | Contents of Rh, Cr and Co on InGaN/ GaN nanowires by ICP-AES test

	Elements	Rh (μg cm^{-2})	Cr (μg cm^{-2})	Co (μg cm^{-2})
Indoor test	Before reaction	5.2	1.9	33.3
	After reaction	2.6	1.9	17.2
Outdoor test	Before reaction	5.8	1.6	62.3
	After reaction	4.6	1.7	42.3

Article

Extended Data Table 2 | Pressure changes contributed by water vapour, hydrogen and oxygen before and after reaction in photocatalytic overall water splitting at different reaction temperature under 3,800 mW cm⁻²

Temperature (°C)		Pressure (kPa)			
		Water vapor	H₂	O₂	Total
30	Before	4.2	0	0	4.2
	After	4.2	1.0	0.5	5.7
40	Before	7.4	0	0	7.4
	After	7.4	2.3	1.3	10.9
50	Before	12.4	0	0	12.4
	After	12.4	6.9	3.1	22.4
60	Before	19.9	0	0	19.9
	After	19.9	15.4	7.4	42.7
70	Before	31.2	0	0	31.2
	After	31.2	24.5	12.7	68.4
80	Before	47.4	0	0	47.4
	After	47.4	24.5	12.1	84.0

The partial pressure of water vapour was calculated by the saturated vapour pressure of water. The partial pressure of hydrogen and oxygen was calculated by their contents in the chamber.

Extended Data Table 3 | List of some state-of-the-art unassisted photocatalytic OWS systems

Photocatalysts	Cocatalysts	Light source	STH (%)	Stability	Year [Ref.]
InGaN/GaN nanowires	Rh/Cr$_2$O$_3$, Co$_3$O$_4$	Xe lamp with AM1.5G filer	9.2	74 h	This work
InGaN/GaN nanowires	Rh/Cr$_2$O$_3$, Co$_3$O$_4$	Natural solar light	6.2	140 min	This work
CoO nanoparticles	N/A	Xe lamp with AM1.5G filer	5	0.5 h	2014 [52]
InGaN/GaN nanowires	Rh/Cr$_2$O$_3$, Co$_3$O$_4$	Xe lamp with AM1.5G filer	1.9	3 h	2018 [5]
Mo:BiVO$_4$-TiO$_2$/CH$_3$NH$_3$PbI$_3$	Pt, CoCO$_3$	Xe lamp with AM1.5G filer	3.0	12 h	2015 [53]
InGaN/GaN nanowires	Rh/Cr$_2$O$_3$	Xe lamp with AM1.5G filer	1.8	10 h	2015 [14]
P-doped g-C$_3$N$_4$ (PCN)	Co$_1$-P$_4$	Xe lamp with AM1.5G filer	0.16	24 h	2017 [54]
Si/TiO$_2$ nano-tree array	Pt-IrO$_x$	Xe lamp with AM1.5G filer	0.12	4.5 h	2013 [55]
Y$_2$Ti$_2$O$_5$S$_2$ nanoparticles	Rh/Cr$_2$O$_3$, IrO$_2$	Xe lamp with AM1.5G filer	0.007	20 h	2019[56]
SrTiO$_3$:La/Au/BiVO$_4$:Mo sheet	Rh, Ru/Cr$_2$O$_3$/TiO$_2$	Xe lamp with AM1.5G filer	1.1	10 h	2016[10]
SrTiO$_3$:Al	Rh/CrO$_x$, CoO$_y$	Natural solar light	0.76	0.5 h	2021[22]
SrTiO$_3$:Al	Rh/CrO$_x$, CoO$_y$	Natural solar light	0.4	0.5 h	2018[4]

Article

Extended Data Table 4 | Free-energy (eV) evolution of reaction steps in hydrogen–oxygen recombination on the cocatalyst Co$_3$O$_4$, Rh and Cr$_2$O$_3$

Catalyst	*	*O$_2$	*O$_2$+H$_2$	*O$_2$H+H	*OH$_2$+O	*O	*O+H$_2$	*OH+H	*OH$_2$	*
Co$_3$O$_4$	0	-2.02	-2.06	-3.07	-4.81	-4.95	-5.44	-5.99	-6.67	-5.64
Rh	0	-2.07	-2.06	-3.45	-3.96	-3.85	-4.47	-4.99	-5.74	-5.64
Cr$_2$O$_3$	0	-1.79	-1.87	-3.01	-5.80	-5.97	-6.37	-6.21	-6.60	-5.64